JOURNAL OF SYNCHROTRON RADIATION
ISSN 1600-5775

In situ electrochemical high-energy X-ray diffraction using a capillary working electrode cell geometry

Matthias J. Young,[a]*‡ Nicholas M. Bedford,[a]*§ Naisheng Jiang,[b] Deqing Lin[b] and Liming Dai[b]

[a]Applied Chemicals and Materials Division, National Institute of Standards and Technology, Boulder, CO 80305, USA, and [b]Center of Advanced Science and Engineering for Carbon (Case4Carbon), Department of Macromolecular Science and Engineering, Case Western Reserve University, Cleveland, OH 44106, USA.
*Correspondence e-mail: matthias.young@anl.gov, nicholas.bedford.ctr@us.af.mil

Received 13 December 2016
Accepted 26 April 2017

Edited by V. Favre-Nicolin, CEA and Université Joseph Fourier, France

‡ Present address: Energy Systems, Argonne National Laboratory, Argonne, IL 60439, USA.
§ Present address: Materials and Manufacturing Directorate, Air Force Research Laboratory, Wright-Patterson AFB, OH 45433, USA.

Keywords: electrochemistry; atomic structure; flow cell; nanoparticles; pair distribution function.

The ability to generate new electrochemically active materials for energy generation and storage with improved properties will likely be derived from an understanding of atomic-scale structure/function relationships during electrochemical events. Here, the design and implementation of a new capillary electrochemical cell designed specifically for *in situ* high-energy X-ray diffraction measurements is described. By increasing the amount of electrochemically active material in the X-ray path while implementing low-Z cell materials with anisotropic scattering profiles, an order of magnitude enhancement in diffracted X-ray signal over traditional cell geometries for multiple electrochemically active materials is demonstrated. This signal improvement is crucial for high-energy X-ray diffraction measurements and subsequent Fourier transformation into atomic pair distribution functions for atomic-scale structural analysis. As an example, clear structural changes in $LiCoO_2$ under reductive and oxidative conditions using the capillary cell are demonstrated, which agree with prior studies. Accurate modeling of the $LiCoO_2$ diffraction data using reverse Monte Carlo simulations further verifies accurate background subtraction and strong signal from the electrochemically active material, enabled by the capillary working electrode geometry.

1. Introduction

Electrochemically active materials are poised to enable significant technological advancements in energy conversion and energy storage through the development of catalysts and electrode layers in fuel cells, batteries and supercapacitors (Winter & Brodd, 2004; Nie *et al.*, 2015; Goriparti *et al.*, 2014; Roy & Srivastava, 2015; Zhi *et al.*, 2013). While development to date is encouraging, new materials with improved properties are needed to compete with and eventually supplant current technologies. Rigorous structure/function relationship development is expected to enable rational design of materials with improved electrochemical properties. In particular, understanding atomic-scale structural changes during electrochemical events can help establish a mechanistic understanding of electrocatalytic reactions and/or charge storage phenomena, as well as provide insights into material longevity (Young *et al.*, 2015, 2016). Recent developments using *in situ* liquid cell transmission electron microscopy (TEM) have demonstrated structural, chemical and morphological changes of active materials under applied bias (Gu *et al.*, 2013; Abellan, Mehdi *et al.*, 2014; Zhu *et al.*, 2014). Though these studies are insightful, electron microscopy is statistically limited by both

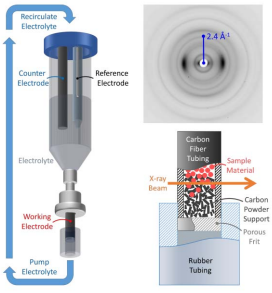

the number of measurements that can reasonably be performed and the amount of material subsequently characterized, and thus may not represent the materials properties observed on an ensemble average collection of material. Additionally, electron-beam-induced processes are often observed and can complicate subsequent analysis (Abellan, Woehl *et al.*, 2014; Woehl *et al.*, 2013).

To obtain a more statistically accurate representation of atomic-scale structure of a material during electrochemical events, *in situ* X-ray based characterization methods have proven to be greatly beneficial. In particular, *in situ* electrochemical X-ray absorption spectroscopy (XAS) has been used to correlate changes in local atomic coordination and bond lengths to electrochemically driven transformations (Gorlin *et al.*, 2013; Nowack *et al.*, 2016; Becknell *et al.*, 2015). However, XAS can only provide structural information within the first coordination sphere of the probed element, potentially complicating subsequent structural modeling. For example, face-centered cubic and hexagonal close-packed lattices exhibit a first coordination sphere of 12 and thus are indistinguishable with XAS. High-energy X-ray diffraction (HE-XRD) coupled with atomic pair distribution function (PDF) analysis can provide much longer-range (>10 nm) (Proffen *et al.*, 2003) structural information than XAS through the Fourier transformation of diffraction data taken at sufficiently high reciprocal space vectors into a function of real-space atomic pair distances. Atomic modeling of PDFs derived from HE-XRD patterns can then be used to assess structure/function relationships (Prasai *et al.*, 2015; Petkov *et al.*, 2008; Bedford *et al.*, 2015; Doan-Nguyen *et al.*, 2014). PDF analysis can be performed on any material irrespective of the level of long-range structural coherence as both diffuse and Bragg components of the diffraction pattern are considered (Billinge & Kanatzidis, 2004; Petkov, 2008). This is particularly advantageous for nanoscale materials, which often exhibit both Bragg-like and diffuse features in their corresponding diffraction patterns due to the lack of long-range order which is inherent to nanomaterials.

Despite the valuable information that can be gained from HE-XRD measurements, fewer *in situ* electrochemical studies have been performed using HE-XRD than XAS. This can be partially explained by the challenge of designing *in situ* cells for HE-XRD measurements *versus* for XAS measurements. XAS is element-specific, and the background signal from the cell can be minimized by appropriately choosing the cell material and electrolyte with little need to optimize the cell geometry. In contrast, during HE-XRD measurements, everything in the path of the incident X-rays (both Bragg and diffuse scattering materials) contributes to the raw diffraction pattern. As such, the signal from the electrochemically active material over the background scales with the relative quantity of the active material and its relative X-ray scattering factor compared with all the components (electrolyte, substrate, electrical contacts, *etc.*) present in the X-ray path through the electrochemical cell. Reducing diffraction from these other components complicates *in situ* cell design and subsequent experimentation.

In situ electrochemical PDF analysis has been reported, however, most notably from *in situ* battery cycling experiments from Sector 11 at the Advanced Photon Source (Hu *et al.*, 2013; Jung *et al.*, 2015; Chupas *et al.*, 2008; Borkiewicz *et al.*, 2015) and recent *in situ* electrocatalytic experimentation reported by Professor Valeri Petkov and colleagues (Petkov *et al.*, 2016; Tuaev *et al.*, 2013; Wu *et al.*, 2015). While these reports illustrate the utility and importance of atomic PDF analysis for *in situ* electrochemical experimentation, readily available *in situ* cells (Figs. 1*a*, 1*b*) have not been optimized for HE-XRD measurements, and thus the material systems investigated have been limited to those with sufficient scattering to obtain usable HE-XRD data for PDF analysis.

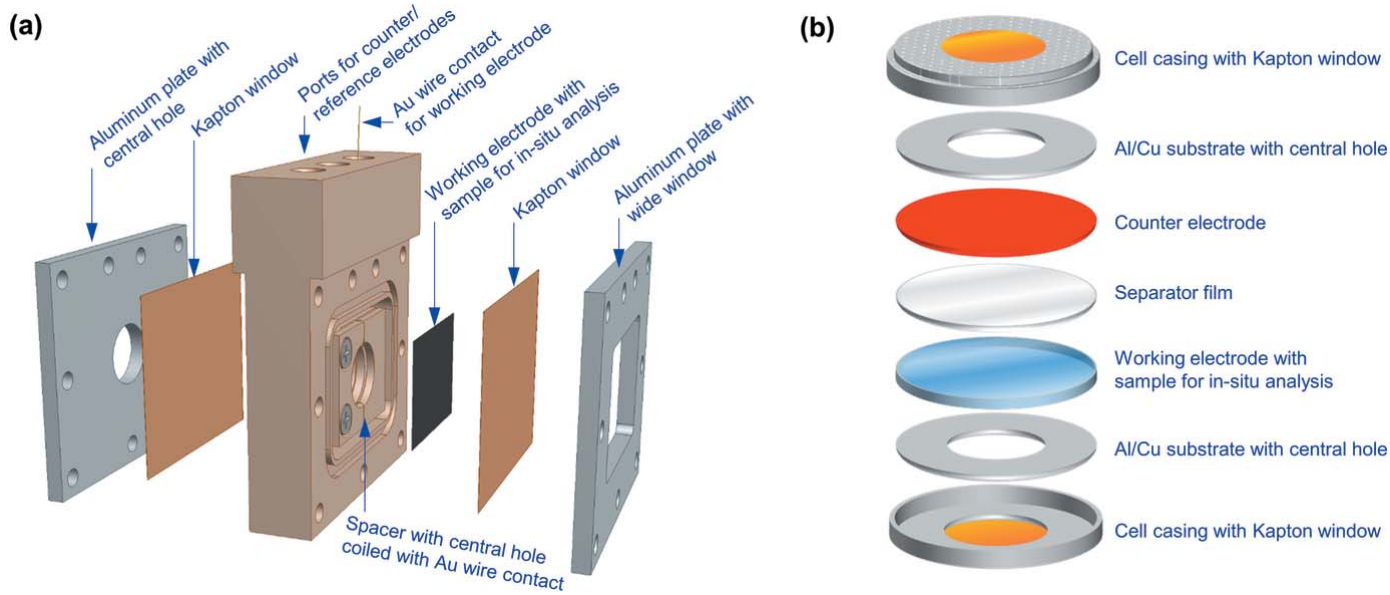

Figure 1
Prototypical *in situ* electrochemical cells: (*a*) a three-electrode half-cell configuration; and (*b*) coin cell configuration for battery cycling experiments.

Depending on the particular application and active material, experimentation with existing *in situ* electrochemical cells may not be feasible. In addition, attempts to increase the amount of active material can result in poor electrical connectivity to the active material and/or a larger fraction of electrochemically inactive materials, making the interpretation of *in situ* data sets more problematic.

In response to the aforementioned issues associated with *in situ* electrochemical HE-XRD measurements, we report on a new *in situ* electrochemical cell design based on an aligned carbon fiber capillary working electrode. This geometry consists of a three-electrode half-cell and improves sample scattering by maximizing sample amount in a capillary environment, similar to commonly performed *ex situ* HE-XRD measurements. Electrolyte volume is minimized to reduce background scattering and constantly recirculated to ensure constant replenishment of reactive species. In addition, the use of an aligned carbon fiber capillary working electrode takes advantage of tight manufacturing tolerances to provide a consistent background between measurements, and results in a largely oriented background scattering that can be readily masked out of the diffraction pattern during image processing without losing structural information at equivalent q-space values. Using various examples, we illustrate the improvement in signal to noise using this capillary cell *versus* comparable traditional *in situ* cells, and demonstrate the ability to probe electrochemically active materials *in situ* using PDF analysis.

2. Experimental

2.1. X-ray measurements

HE-XRD data reported in this paper were collected at 11-ID-B, 11-ID-C and 6-ID-D at the Advanced Photon Source (APS), Argonne National Laboratory, using 58.65, 105 and 100 keV irradiation, respectively. All experiments were performed in a transmission geometry with a sample-to-detector distance to maximize the sampled q-range. Where applicable, HE-XRD data were background-corrected, converted into total structure functions and Fourier transformed into their corresponding atomic PDFs using *PDFgetX3* (Juhás *et al.*, 2013). Reverse Monte Carlo (RMC) calculations were performed to analyze the PDFs collected for $LiCoO_2$ using the *fullrmc* Python package (Aoun, 2016).

2.2. Materials

Fe–Ni layered double hydroxide (LDH) aqueous nanoparticles suspensions were synthesized using co-precipitation (Cavani *et al.*, 1991) of $FeCl_3$ (Spectrum; minimum 98%) and $NiCl_2{\cdot}6H_2O$ (Amresco; high purity) in 0.15 *M* NaOH (EMD Millipore; ACS grade) under a continuous argon purge (AirGas; UHP), resulting in a nanoparticle concentration of ~1 wt%. For use in the half-cell design in Fig. 1(*a*), Fe–Ni LDH nanoparticles were dropcast onto carbon paper (see below). For use in the capillary cell in Fig. 2, Fe–Ni LDH nanoparticles were lyophilized and crushed to obtain a powder. Pt nanoparticles on multi-walled carbon nanotubes

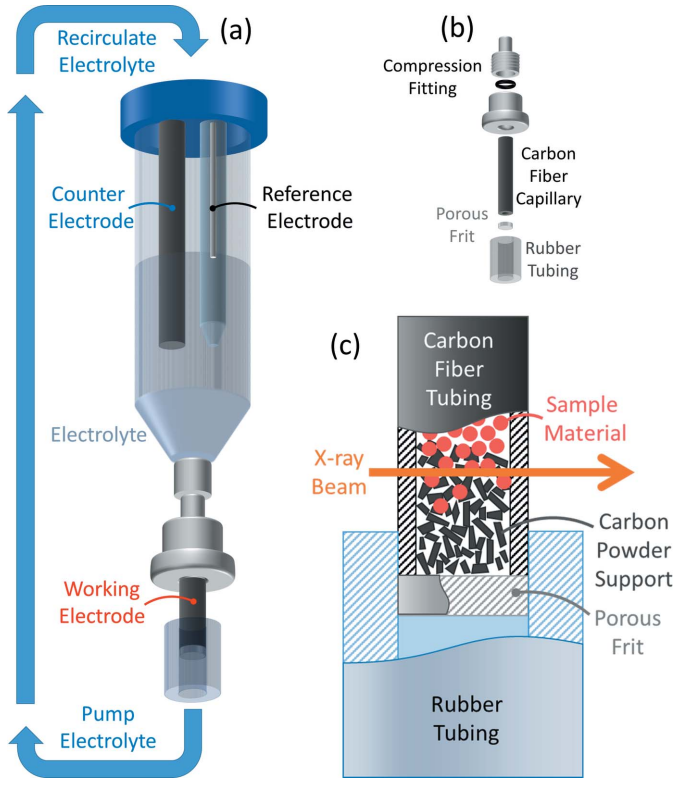

Figure 2
Schematic of the capillary *in situ* electrochemical cell, including: (*a*) an overall schematic of the cell, containing the epoxy-aligned carbon fiber capillary working electrode connected to an electrolyte reservoir containing the counter electrode, and reference electrode. Electrolyte is recirculated *via* peristaltic pump to replenish the electrolyte species; (*b*) the components connecting the working electrode to the electrolyte reservoir; and (*c*) schematic of the interior of the working electrode, containing amorphous carbon powder support for the electrochemically active material.

(MWCNTs) or graphene sheets were synthesized by chemical co-reduction of potassium tetrachloroplatinate(II) (K_2PtCl_4, ≥99.9%, Sigma Aldrich) along with graphene oxide (GO) sheets or surface-oxidized MWCNTs in aqueous ethylene glycol (EG) solutions (Li *et al.*, 2010; Hu *et al.*, 2012). Here, the pristine GO nanosheets were synthesized using the well-established modified Hummers' methods (Xue *et al.*, 2012; Kovtyukhova *et al.*, 1999). The surface-oxidized MWCNTs were synthesized *via* direct oxidation with HNO_3 (Xing, 2004). In brief, the uniformly dispersed K_2PtCl_4/GO/EG or K_2PtCl_4/surface-oxidized MWCNT/EG solutions with an adjusted pH of 13 were heated at 120°C for 4–12 h under magnetic stirring. After the reduction reaction, the final Pt–graphene or Pt–MWCNT composites were filtered and thoroughly washed with ethanol and de-ionized water, and further dried in a vacuum desiccator. $LiCoO_2$ powder (97%) was purchased from Alfa Aesar and used as received.

2.3. Electrochemical measurement

During *in situ* electrochemical HE-XRD experimentation, electrochemical measurements were performed in a three-electrode configuration using a SP-300 potentiostat (Biologic),

controlled with *EC-Lab* software (Biologic). A saturated Ag/AgCl reference electrode (BASi) and graphite rod counter electrode (Princeton Applied Research) were employed in both the half-cell and capillary working electrode cells described below. Unless otherwise indicated, a 1 *M* NaOH electrolyte was used for electrochemical measurements, and a continuous oxygen purge was maintained throughout operation.

3. Cell design and operation

3.1. Traditional cell designs

As described in the *Introduction*, many of the existing cells used to collect *in situ* electrochemical HE-XRD data have not been optimized for X-ray diffraction. For instance, the three-electrode half-cell depicted in Fig. 1(*a*) was designed for XAS measurements (McBreen *et al.*, 1987). In this cell, the active material is commonly dropcast or pressed into a low-*Z* substrate resulting in a total active material thickness of the order of 10–100 µm. Here, we employ a non-woven carbon fiber paper (Fuel Cell Earth; Toray carbon paper, thickness ∼300 µm) substrate. This carbon fiber paper is compressed against a coiled Au wire by bolting Kapton-covered aluminium windows on either side of the cell. For fluorescent XAS measurements, the active material is placed adjacent to a large window in the aluminium plate, and the cell is angled between the X-ray beam and the fluorescent detector. This cell is well designed for this purpose, and allows for convenient operation and good signal in fluorescent XAS measurements. However, when used for X-ray diffraction measurements, the half-cell's limited capacity for active material and comparatively long X-ray path length through the electrolyte and carbon fiber paper produce low signal with diffuse noise arising from the electrolyte. Furthermore, the Kapton windows in the cell are flexible, and conform to the sample, making it difficult to obtain a consistent background between X-ray diffraction measurements (Borkiewicz *et al.*, 2012). These aspects of the design are inconsequential for fluorescent XAS measurements, but make high-resolution HE-XRD measurements challenging, and in many cases preclude the use of PDF analysis.

Another common implementation configures the electrochemical cell geometry such that the active component under investigation is stacked with the remaining device materials, such as a membrane electrode assembly for electrocatalyst testing (Sasaki *et al.*, 2016; McBreen *et al.*, 1987) or coin cell for battery/supercapacitor testing (Richard *et al.*, 1997). The coin cell design, as depicted in Fig. 1(*b*), emerged from the prevalence of coin cells in lithium ion battery research (Richard *et al.*, 1997) and was also not designed to optimize the X-ray diffraction signal. This cell uses conventional coin cell hardware, and adds low-*Z* windows (*e.g.* Kapton) to the coin cell casing, and center holes to the current collectors to allow for X-ray transmission. For the battery community, this design allows for convenient construction of an *in situ* X-ray diffraction cell. However, this cell geometry also limits the amount of active material which can be loaded into the cell, and the flexible Kapton windows lead to the same difficulties for obtaining a consistent background between measurements as discussed above (Borkiewicz *et al.*, 2012). This design also requires that the diffraction signal from the counter electrode be subtracted for the measurements, or that a window be cut through the counter electrode. While many of these issues have been addressed with recent improvements to this cell design (Borkiewicz *et al.*, 2012; Wilson *et al.*, 2014; Roberts & Stewart, 2004; Braun *et al.*, 2003), the coin cell geometry limits the possible electrochemical systems which can be studied. The coin cell geometry does not conveniently allow for the use of a reference electrode, and requires that the process taking place on the working electrode be balanced by an equivalent process on the counter electrode.

3.2. Capillary working electrode cell

Here, we report a new electrochemical cell with a capillary working electrode designed specifically for *in situ* X-ray diffraction measurements. The working electrode design is inspired by the capillaries commonly used in *ex situ* HE-XRD measurements, and allows for a higher mass of active material and minimal electrolyte volume in the X-ray path. This provides dramatic signal enhancement over existing cell designs and enables PDF analysis for electrochemical systems where previous cell designs have proven to be problematic. A schematic of the cell is presented in Fig. 2. Fig. 2(*a*) shows the overall layout of the cell, with a counter and reference electrode in an electrolyte reservoir, and the capillary working electrode at the base of the reservoir. Fresh electrolyte is continually supplied to the working electrode by pulling electrolyte from the reservoir through the working electrode using a peristaltic pump, as depicted in Fig. 2(*a*). Recirculation ensures that a continuous supply of electrolyte is available for lengthy measurements. The electrolyte may also be collected for analysis rather than recirculated.

An exploded view of the working electrode is shown in Fig 2(*b*). The outer wall of the working electrode is a low-*Z* electrically conductive capillary. Here, we employ an epoxy-aligned carbon fiber capillary (0.125" OD; ACP Composites). Tight manufacturing tolerances [here 0.125" + 0.000"/0.003" OD and 0.072" ± 0.003" ID (ACP Composites Inc., 2016)] on this and equivalent carbon fiber capillaries provide a consistent background between measurements, while the aligned carbon fibers result in a largely anisotropic background, which is readily masked out during processing of the diffraction data. The capillary working electrode is attached to the electrolyte reservoir with a compression fitting. The compression fitting allows for rapid swapping of capillaries, enabling more efficient operation when analyzing an array of samples. The carbon fiber capillary is electrically isolated from the compression fitting using an electrically insulating O-ring. The active material in the carbon fiber capillary rests on a porous frit, here a polyethylene frit with 20 µm porosity, which is held in place using fitted rubber tubing. The specific technique for loading the capillary can be tuned for a given material system.

Here, we chose to add conductive granular activated carbon (Norit GAC 400M-1746) to the carbon fiber capillary, and then added active material on top of the carbon as depicted in Fig. 2(*c*). The granular activated carbon provides a porous network for the electrolyte to flow through the carbon fiber capillary, and also provides electrical connectivity to the active material. Additional granular activated carbon contributes minimal background to the resulting HE-XRD pattern. An electrical connection was made to the working electrode by attaching an alligator clip to the exterior of the carbon fiber capillary just below the compression fitting.

In order to optimize the diffraction signal from the active material against the electrical connectivity from the carbon powder, we aligned the X-ray beam just below the interface between the carbon powder and active material as depicted in Fig. 2(*c*). A photograph of a prototype capillary working electrode cell is depicted in Fig. 3. Alignment was performed by scanning the cell in the vertical direction (parallel to the axis of the capillary tube) while using a photodiode detector as shown in Fig. 3 to measure the direct X-ray beam intensity (*i.e.* unscattered X-rays). The photodiode showed a high X-ray intensity when scanning the X-ray beam over the low-*Z* granular activated carbon, and a drop in X-ray intensity when the X-ray beam was positioned over the higher-*Z* active material. The vertical cell position was adjusted to the inflection point in the photodiode signal to ensure that a blend of active material and conductive carbon support were in the X-ray path. Finally, the cell position was fine-tuned with the photodiode removed to optimize the scattering from the active material as measured directly from the X-ray area detector.

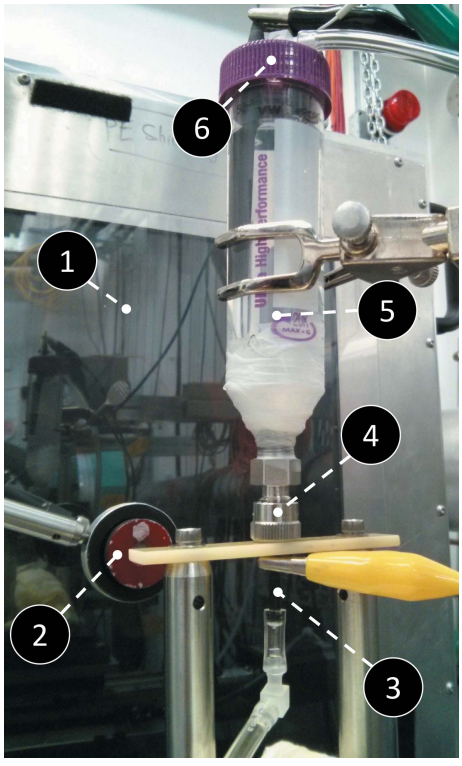

Figure 3
Photograph of a prototype *in situ* electrochemical cell with capillary working electrode in operation at 6-ID-D beamline at APS, showing (1) two-dimensional X-ray area detector, (2) photodiode, (3) carbon fiber capillary working electrode, (4) compression fitting, (5) electrolyte reservoir, and (6) ports with counter electrode, reference electrode and tubing for electrolyte recirculation.

4. Results and discussion

To demonstrate the enhancement in signal from the electrochemically active materials and the ability to perform *in situ* electrochemical HE-XRD measurements to obtain subsequent atomic PDFs using the capillary working electrode cell, we perform HE-XRD measurements on a series of example materials. We contrast the X-ray diffraction signal obtained with our capillary working electrode cell geometry (Figs. 2 and 3) against the signal obtained using the traditional half-cell geometry (Fig. 1*a*) for lower-*Z* transition-metal hydroxide nanoparticles (Fe–Ni LDHs) and high-*Z* platinum nanoparticles on nanocarbon supports. While these two material systems serve the purpose of contrasting the diffraction signal over the background between the cell geometries, atomic structure changes during electrochemical operation have not been well characterized for these materials. In order to verify the ability to accurately determine structural changes under electrochemical operation using the capillary working electrode cell, we perform HE-XRD measurements on commercial $LiCoO_2$ powder using the capillary working electrode cell and compare the structural changes we observe with prior studies on $LiCoO_2$.

In general, LDH nanoparticles have shown promise for a range of applications including energy conversion (Sels *et al.*, 1999; Song & Hu, 2014), energy storage (Chen *et al.*, 2014; Gong *et al.*, 2014) and drug delivery (Choy *et al.*, 2000). Here, electrocatalytic Fe–Ni LDH nanoparticles (Long *et al.*, 2014, 2015) are used to showcase the improvement of active material scattering visually from the transmitted X-ray diffraction patterns in Fig. 4. For use in a traditional half-cell geometry (Fig. 1*a*), Fe–Ni LDH nanoparticles were deposited onto a non-woven carbon fiber working electrode for *in situ* electrochemical experiments. The diffraction patterns for a bare carbon paper, and carbon paper with Fe–Ni LDH nanoparticles in the assembled half-cell geometry with electrolyte are shown in Figs. 4(*a*) and 4(*b*), respectively. The white object oriented diagonally in Figs. 4(*a*) and 4(*b*) is a beam-stop. Only a faint diffraction ring arising from the Fe–Ni LDH nanoparticles can be seen around the center black circle in Fig. 4(*b*). This diffraction ring has an intensity which is only 2.7% larger than the background signal. The minimal differences observed in the diffraction patterns in Figs. 4(*a*) and 4(*b*) highlight the poor signal from the active material in the traditional half-cell geometry. Given the relative amount of Fe–Ni LDH nanoparticles in comparison with the background materials (Kapton windows, carbon fiber working electrode and electrolyte), the small signal from the active material is to be expected. Only when nanomaterials containing sufficiently

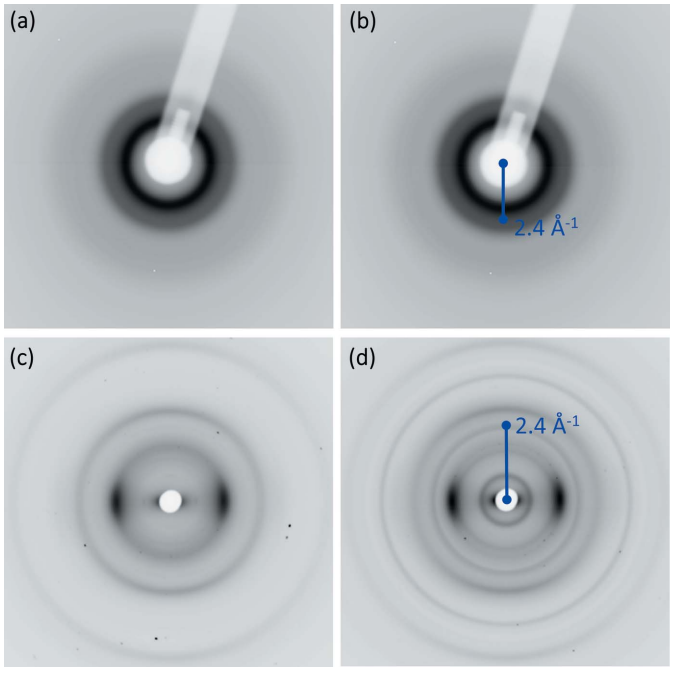

Figure 4
HE-XRD patterns for Fe–Ni LDH nanoparticles using two different *in situ* cell configurations: (*a*) conventional three-electrode half-cell without Fe–Ni LDH nanoparticles; (*b*) conventional three-electrode half-cell with Fe–Ni LDH nanoparticles; (*c*) aligned carbon fiber *in situ* cell without Fe–Ni LDH nanoparticles; and (*d*) aligned carbon fiber *in situ* cell with Fe–Ni LDH nanoparticles. HE-XRD from (*a*) and (*b*) were obtained at 11-ID-B (58.65 keV) while (*c*) and (*d*) were obtained at 6-ID-D (100 keV).

high-Z elements are used will the diffraction signal be measureable above the background scattering of the cell (such as Pt, see below). This severely limits the use of this traditional configuration to study materials based on first-row transition metals, which is a staggering limitation given the earth abundance of first-row transition metals, and their corresponding prevalence in emerging electrochemical research (Cottineau *et al.*, 2006; Poizot *et al.*, 2000; Burke *et al.*, 2015).

To evaluate the signal improvement with the capillary working electrode geometry, Fe–Ni LDH nanoparticles were loaded into an aligned carbon fiber capillary with granular carbon and inserted into the capillary working electrode cell, as described above. The resulting diffraction patterns for an empty carbon capillary and a capillary with Fe–Ni LDH nanoparticles in the assembled capillary working electrode cell geometry with electrolyte are shown in Figs. 4(*c*) and 4(*d*), respectively. The capillary working electrode geometry yielded dramatically improved scattering from the nanoparticles over the background of the cell. Multiple diffraction rings from the Fe–Ni LDH nanoparticles are evident in Fig. 4(*d*). The primary diffraction ring at 2.4 $Å^{-1}$ has an intensity which is 38% larger than the background signal, corresponding to a 14-fold signal improvement over the half-cell geometry. The capillary working electrode geometry results in minimal background scattering while increasing the path length of active material probed by the X-rays, such that sufficient signal can be extracted from the background for subsequent PDF analysis. Furthermore, the Bragg diffraction from the carbon fiber working electrode in Fig. 4(*c*) is oriented due to the alignment of carbon fibers in the as-processed capillaries. The most visible component of this Bragg diffraction is two vertically elongated black ovals seen in the horizontal diffraction direction, which are symmetric about the center of the pattern. The oriented background from the aligned carbon fibers is also visible in Fig. 4(*d*). This largely oriented background can easily be masked out of the diffraction pattern during image processing, allowing for improved background subtraction, which is particularly useful when examining materials with similarly positioned diffraction peaks to carbon fibers.

Examination of Pt nanoparticle scattering from both cell geometries in Fig. 5 further demonstrates the improved scattering achievable with the capillary working electrode geometry. The diffraction patterns in Fig. 5 are integrated *via* image processing from diffraction patterns analogous to those presented in Fig. 4. Pt nanoparticles are established electro-

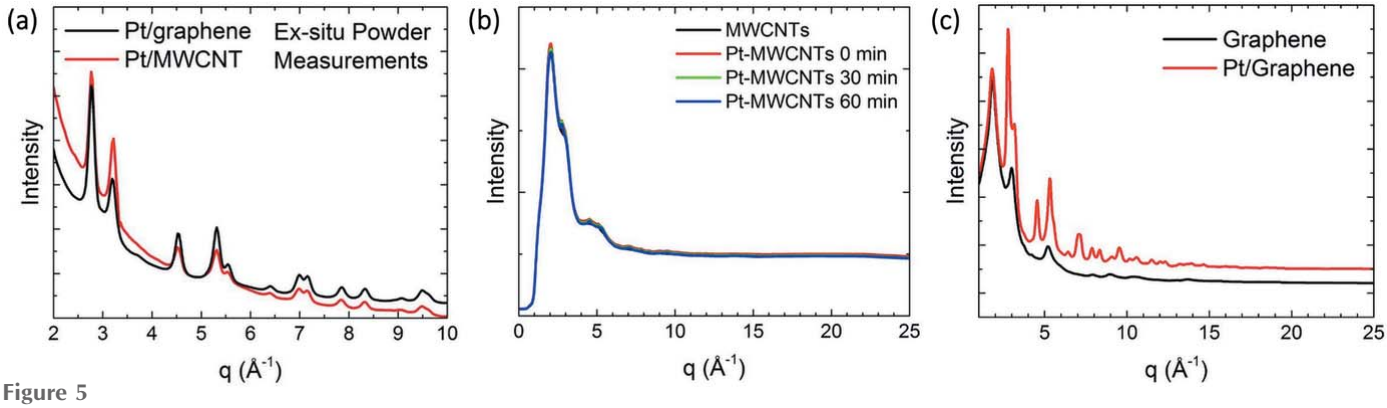

Figure 5
Raw HE-XRD patterns for Pt nanoparticles (*a*) in *ex situ* Kapton capillaries, (*b*) in a three-electrode half-cell geometry at open circuit voltage (OCV) (red line), cycled for 30 min (green line) and 60 min (blue line) as compared with a background MWCNT pattern, and (*c*) in an aligned carbon fiber working electrode geometry at OCV (red line) compared with the background graphene pattern (black line). HE-XRD patterns for the *ex situ* Kapton capillaries were recorded at the 11-ID-C station (105 keV) at APS. HE-XRD patterns for the three-electrode hall-cell geometry were recorded at the 11-ID-B station (58.65 keV) at APS. HE-XRD patterns from the aligned carbon fiber working electrode geometry were recorded at the 6-ID-D station (100 keV) at APS.

catalysts (Curnick *et al.*, 2012; Lee *et al.*, 2006) and serve as a good comparison material between the electrochemical cells given that Pt is a high-Z material that strongly scatters X-rays. In Fig. 5(*a*), the scattering intensity signal is shown to be equivalent for Pt on MWCNTs and graphene when measured *ex situ* in Kapton capillaries with equivalent amounts of probed material. Using a three-electrode half-cell geometry (Fig. 1*a*), scattering from Pt nanoparticles deposited on MWCNTs results in very small Bragg peaks that at most are only ∼1% above the background scattering (Fig. 5*b*). Minor changes in HE-XRD patterns are noted in the Pt nanoparticles when cycled in 1 *M* NaOH at potentials between 0.1 V and 0.7 V under continuous oxygen purge, yet the scattering intensity remains sufficiently low to preclude PDF analysis. In contrast, Pt nanoparticle deposited on graphene nanosheets clearly exhibit a much higher intensity HE-XRD pattern as compared with the background as depicted in Figs. 5(*c*) and 5(*d*) when using the capillary working electrode geometry (Fig. 2). The primary diffraction peak at 2.74 $Å^{-1}$ has an intensity which is ∼17% above the background, an order of magnitude signal enhancement *versus* the conventional half-cell geometry. Such improvement in intensity over the background provides for a more accurate background subtraction for subsequent PDF processing and analysis. Modeling of *in situ* Pt nanoparticle PDFs with RMC simulations is expected to obtain atomic-scale structural differences across the length of the nanoparticle during electrochemical cycling (Petkov *et al.*, 2016), and is the subject of future studies.

While specific structural changes for the above systems will be discussed in future reports where adequate context can be given, here we demonstrate the electrochemical operation of the capillary working electrode cell geometry using $LiCoO_2$, a common cathode material for lithium ion batteries. The electrochemical behavior of $LiCoO_2$ has been studied using *in situ* XRD (Reimers & Dahn, 1992), TEM (Wang *et al.*, 1999) and electrochemical quartz crystal microbalance (Choi *et al.*, 1998) techniques. The operation of $LiCoO_2$ as an electrode for lithium ion batteries has been explored in both non-aqueous (Plichta *et al.*, 1989) and aqueous (Ruffo *et al.*, 2009) electrolytes. At potentials more positive than 3.9 V *versus* Li/Li^+ (0.7 V *versus* Ag/AgCl), Li is expelled from the $LiCoO_2$ structure, forming $Li_{1-x}CoO_2$ and leading to structural differences which are discernable by X-ray diffraction (Ruffo *et al.*, 2009; Plichta *et al.*, 1989; Reimers & Dahn, 1992). On reverse polarization, the Li^+ incorporates back into the $Li_{1-x}CoO_2$ structure, reforming $LiCoO_2$.

During *in situ* measurements on $LiCoO_2$ in this work, the $LiCoO_2$-containing working electrode was repeatedly cycled between +1 V (oxidation) and −1 V (reduction) *versus* Ag/AgCl for 8 min intervals in an aqueous 0.1 *M* LiCl electrolyte under continuous argon purge. The PDFs for $LiCoO_2$ under oxidation and reduction conditions averaged over three electrochemical cycles are shown in Fig. 6(*a*). We note that the short discharge time of 8 min is expected to result in the removal of only a fraction of the Li^+ from the $LiCoO_2$ structure. Also, the bulk $LiCoO_2$ powder used here is expected to exhibit modest structural changes compared with nanoscale electrode materials of interest to next-generation batteries. Nonetheless, we do observe statistically significant structural differences (exceeding two standard deviations) in the PDFs under different applied biases (see below for discussion).

We also performed RMC modeling on the PDF data as shown in Fig. 6(*b*) using a pristine $LiCoO_2$ starting structure (Aoun, 2016). This modeling consisted of $>10^7$ RMC steps, including atomic translations, Li-Co swaps and removal of Li. Despite the impurities and defects expected to be present in commercially available bulk $LiCoO_2$ powder, we see mostly good agreement between the experimental data and model

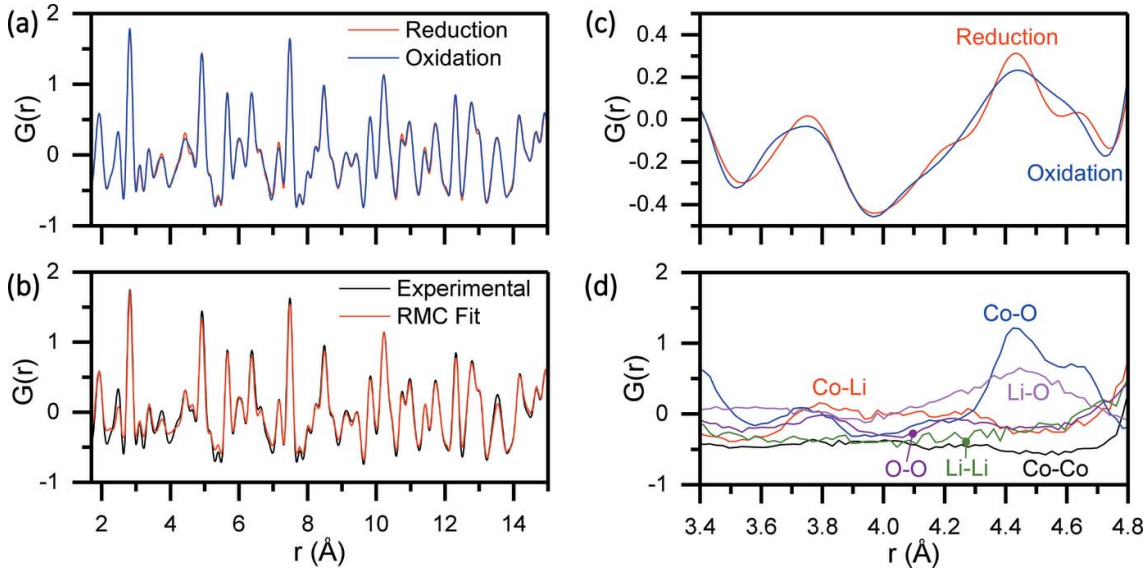

Figure 6
(*a*) Pair distribution function calculated from *in situ* HE-XRD data for $LiCoO_2$ in an aligned carbon fiber working electrode geometry for measurements taken under oxidizing and reducing potentials averaged over three cycles. (*b*) RMC fit of the reduction data in (*a*) using a bulk $LiCoO_2$ starting structure. (*c*) A zoomed window of (*a*) highlighting changes measured under applied bias. (*d*) A species decomposed intensity from the reduction potential fit in (*b*) over the region highlighted in (*c*). Experiments were performed at the 6-ID-D beamline at APS.

based on pristine $LiCoO_2$. We note that the RMC modeling does not fully capture the experimental PDF at pair distances between 2 and 5 Å. This pair distance range is expected to correspond to first and second coordination sphere metal–oxygen and metal–metal pairs, as supported by the partial $G(r)$ traces in Fig. 6(*d*). We expect that local variations in the atomic structure and composition in the commercial $LiCoO_2$ used here give rise to the disparity between the experimental PDF and the RMC model. Overall close agreement of experimental data with the $LiCoO_2$ model indicates that a sufficiently large active material diffraction signal and reproducible background can be obtained using the capillary cell to provide accurate structural information. We note that uncertainty in the RMC modeled structure points to an incomplete description of the exact atomic structure, but still allows for a qualitative interpretation of the statistically significant structural changes observed experimentally.

Prior work has suggested that lithium removal from $LiCoO_2$ leads to structural differences in the region surrounding an atomic pair distance of ~4.7 Å (Reimers & Dahn, 1992). This region of Fig. 6(*a*) is highlighted in Fig. 6(*c*), and we observe structural differences as a function of applied bias using the capillary working electrode cell geometry which are in agreement with these previous results. Furthermore, the pair-decomposed partial $G(r)$ traces calculated using the *Interactive Structure Analysis of Amorphous and Crystalline Systems* (*ISAACS*) program (Le Roux & Petkov, 2010) as shown in Fig. 6(*d*) suggest that the changes to the PDF in Fig. 6(*c*) arise primarily from changing Co–O distances, which is consistent with prior reports (Wang *et al.*, 1999; Reimers & Dahn, 1992). These structural shifts have been attributed to a canting of the *c*-axis in the hexagonal $LiCoO_2$ structure (Reimers & Dahn, 1992) and the formation of exchange defects between Co and Li (Wang *et al.*, 1999). While further analysis and interpretation of the structural changes is outside the scope of this paper, the promise of new structural information from *in situ* PDF analysis enabled by our capillary working electrode cell geometry is demonstrated with the $LiCoO_2$ data we present here.

5. Conclusion

The described capillary working electrode electrochemical cell geometry was designed to address issues with scattering intensity and reproducible background signal for *in situ* HE-XRD measurements. The use of a capillary working electrode is beneficial for three reasons: (i) it allows for easy loading of appreciable amounts of material to provide sufficient scattering over the background signal; (ii) the background signal from the carbon capillary has low variability, arising from tight manufacturing tolerances; (iii) as the capillary consists of aligned carbon fiber, the majority of the scatter background is anisotropic, which can readily be masked out of the two-dimensional diffraction pattern during image processing. Using a series of examples, we have demonstrated the utility of this cell for enhancing the HE-XRD signal by an order of magnitude for *in situ* electrochemical measurements on various material systems. The improved resolution in HE-XRD data afforded by the capillary cell geometry will enable PDF analysis for a range of electrochemical systems where this has not been possible before. PDF analysis on these systems will help to improve understanding of structural changes during electrochemical events and to establish structure/function relationships for electrochemical technologies, driving a new age of material innovation for electrochemical applications.

Acknowledgements

This research was performed while author MJY held an NRC Research Associateship award at the National Institute of Standards and Technology. This work was performed at 11-ID-C, 11-ID-B and 6-ID-D beamlines of the Advanced Photon Source, a US Department of Energy (DOE) Office of Science User Facility operated for the DOE Office of Science by Argonne National Laboratory under Contract No. DE-AC02-06CH11357. We would like to thank Yang Ren for assistance with experiments at 11-ID-C, Karena Chapman and Kevin Beyer for assistance with experiments at 11-ID-B, and Chris Benmore and Douglas Robinson for assistance with experiments at 6-ID-D.

Funding information

Funding for this research was provided by: National Academy of Sciences (award No. NRC-RAP).

References

Abellan, P., Mehdi, B. L., Parent, L. R., Gu, M., Park, C., Xu, W., Zhang, Y., Arslan, I., Zhang, J., Wang, C., Evans, J. E. & Browning, N. D. (2014). *Nano Lett.* **14**, 1293–1299.
Abellan, P., Woehl, T. J., Parent, L. R., Browning, N. D., Evans, J. E. & Arslan, I. (2014). *Chem. Commun.* **50**, 4873–4880.
ACP Composites Inc. (2016). 125" OD Carbon Fiber Pultruded Tube. ACP Composites Inc., Livermore, CA, USA.
Aoun, B. (2016). *J. Comput. Chem.* **37**, 1102–1111.
Becknell, N., Kang, Y., Chen, C., Resasco, J., Kornienko, N., Guo, J., Markovic, N. M., Somorjai, G. A., Stamenkovic, V. R. & Yang, P. (2015). *J. Am. Chem. Soc.* **137**, 15817–15824.
Bedford, N. M., Ramezani-Dakhel, H., Slocik, J. M., Briggs, B. D., Ren, Y., Frenkel, A. I., Petkov, V., Heinz, H., Naik, R. R. & Knecht, M. R. (2015). *ACS Nano*, **9**, 5082–5092.
Billinge, S. J. L. & Kanatzidis, M. G. (2004). *Chem. Commun.* pp. 749–760.
Borkiewicz, O. J., Shyam, B., Wiaderek, K. M., Kurtz, C., Chupas, P. J. & Chapman, K. W. (2012). *J. Appl. Cryst.* **45**, 1261–1269.
Borkiewicz, O. J., Wiaderek, K. M., Chupas, P. J. & Chapman, K. W. (2015). *J. Phys. Chem. Lett.* **6**, 2081–2085.
Braun, A., Shrout, S., Fowlks, A. C., Osaisai, B. A., Seifert, S., Granlund, E. & Cairns, E. J. (2003). *J. Synchrotron Rad.* **10**, 320–325.
Burke, M. S., Enman, L. J., Batchellor, A. S., Zou, S. & Boettcher, S. W. (2015). *Chem. Mater.* **27**, 7549–7558.
Cavani, F., Trifirò, F. & Vaccari, A. (1991). *Catal. Today*, **11**, 173–301.
Chen, H., Hu, L., Chen, M., Yan, Y. & Wu, L. (2014). *Adv. Funct. Mater.* **24**, 934–942.
Choi, Y.-M., Pyun, S.-I. & Shin, H.-C. (1998). *Met. Mater.* **4**, 193–201.

Choy, J.-H., Kwak, S.-Y., Jeong, Y.-J. & Park, J. (2000). *Angew. Chem. Int. Ed.* **39**, 4041–4045.
Chupas, P. J., Chapman, K. W., Kurtz, C., Hanson, J. C., Lee, P. L. & Grey, C. P. (2008). *J. Appl. Cryst.* **41**, 822–824.
Cottineau, T., Toupin, M., Delahaye, T., Brousse, T. & Bélanger, D. (2006). *Appl. Phys. A*, **82**, 599–606.
Curnick, O. J., Pollet, B. G. & Mendes, P. M. (2012). *RSC Adv.* **2**, 8368–8374.
Doan-Nguyen, V. V. T., Kimber, S. A. J., Pontoni, D., Reifsnyder Hickey, D., Diroll, B. T., Yang, X., Miglierini, M., Murray, C. B. & Billinge, S. J. L. (2014). *ACS Nano*, **8**, 6163–6170.
Gong, M., Li, Y., Zhang, H., Zhang, B., Zhou, W., Feng, J., Wang, H., Liang, Y., Fan, Z., Liu, J. & Dai, H. (2014). *Energ. Environ. Sci.* **7**, 2025–2032.
Goriparti, S., Miele, E., De Angelis, F., Di Fabrizio, E., Proietti Zaccaria, R. & Capiglia, C. (2014). *J. Power Sources*, **257**, 421–443.
Gorlin, Y., Lassalle-Kaiser, B., Benck, J. D., Gul, S., Webb, S. M., Yachandra, V. K., Yano, J. & Jaramillo, T. F. (2013). *J. Am. Chem. Soc.* **135**, 8525–8534.
Gu, M., Parent, L. R., Mehdi, B. L., Unocic, R. R., McDowell, M. T., Sacci, R. L., Xu, W., Connell, J. G., Xu, P., Abellan, P., Chen, X., Zhang, Y., Perea, D. E., Evans, J. E., Lauhon, L. J., Zhang, J. G., Liu, J., Browning, N. D., Cui, Y., Arslan, I. & Wang, C. M. (2013). *Nano Lett.* **13**, 6106–6112.
Hu, C., Cheng, H., Zhao, Y., Hu, Y., Liu, Y., Dai, L. & Qu, L. (2012). *Adv. Mater.* **24**, 5493–5498.
Hu, Y., Liu, Z., Nam, K., Borkiewicz, O. J., Cheng, J., Hua, X., Dunstan, M. T., Yu, X., Wiaderek, K. M., Du, L., Chapman, K. W., Chupas, P. J., Yang, X. & Grey, C. P. (2013). *Nat. Mater.* **12**, 1130–1136.
Juhás, P., Davis, T., Farrow, C. L. & Billinge, S. J. L. (2013). *J. Appl. Cryst.* **46**, 560–566.
Jung, H., Allan, P. K., Hu, Y. Y., Borkiewicz, O. J., Wang, X. L., Han, W. Q., Du, L. S., Pickard, C. J., Chupas, P. J., Chapman, K. W., Morris, A. J. & Grey, C. P. (2015). *Chem. Mater.* **27**, 1031–1041.
Kovtyukhova, N. I., Ollivier, P. J., Martin, B. R., Mallouk, T. E., Chizhik, S. A., Buzaneva, E. V. & Gorchinskiy, A. D. (1999). *Chem. Mater.* **11**, 771–778.
Lee, K., Zhang, J., Wang, H. & Wilkinson, D. P. (2006). *J. Appl. Electrochem.* **36**, 507–522.
Le Roux, S. & Petkov, V. (2010). *J. Appl. Cryst.* **43**, 181–185.
Li, Y., Gao, W., Ci, L., Wang, C. & Ajayan, P. M. (2010). *Carbon*, **48**, 1124–1130.
Long, X., Li, J., Xiao, S., Yan, K., Wang, Z., Chen, H. & Yang, S. (2014). *Angew. Chem. Int. Ed.* **53**, 7584–7588.
Long, X., Xiao, S., Wang, Z., Zheng, X. & Yang, S. (2015). *Chem. Commun.* **51**, 1120–1123.
McBreen, J., O'Grady, W. E., Pandya, K. I., Hoffman, R. W. & Sayers, D. E. (1987). *Langmuir*, **3**, 428–433.
Nie, Y., Li, L. & Wei, Z. (2015). *Chem. Soc. Rev.* **44**, 2168–2201.
Nowack, L., Grolimund, D., Samson, V., Marone, F. & Wood, V. (2016). *Sci. Rep.* **6**, 21479.
Petkov, V. (2008). *Mater. Today*, **11**, 28–38.
Petkov, V., Bedford, N., Knecht, M. R., Weir, M. G., Crooks, R. M., Tang, W., Henkelman, G. & Frenkel, A. (2008). *J. Phys. Chem. C*, **112**, 8907–8911.
Petkov, V., Prasai, B., Shan, S., Ren, Y., Wu, J., Cronk, H., Luo, J. & Zhong, C. (2016). *Nanoscale*, **8**, 10749–10767.
Plichta, E., Slane, S., Uchiyama, M., Salomon, M., Chua, D., Ebner, W. B. & Lin, H. W. (1989). *J. Electrochem. Soc.* **136**, 1865–1869.
Poizot, P., Laruelle, S., Grugeon, S., Dupont, L. & Tarascon, J. (2000). *Nature (London)*, **407**, 496–499.
Prasai, B., Wilson, A. R., Wiley, B. J., Ren, Y. & Petkov, V. (2015). *Nanoscale*, **7**, 17902–17922.
Proffen, T., Billinge, S. J. L., Egami, T. & Louca, D. (2003). *Z. Kristallogr.* **218**, 132–143.
Reimers, J. N. & Dahn, J. R. (1992). *J. Electrochem. Soc.* **139**, 2091.
Richard, M. N., Koetschau, I. & Dahn, J. R. (1997). *J. Electrochem. Soc.* **144**, 554–557.
Roberts, G. A. & Stewart, K. D. (2004). *Rev. Sci. Instrum.* **75**, 1251–1254.
Roy, P. & Srivastava, S. K. (2015). *J. Mater. Chem. A*, **3**, 2454–2484.
Ruffo, R., Wessells, C., Huggins, R. A. & Cui, Y. (2009). *Electrochem. Commun.* **11**, 247–249.
Sasaki, K., Marinkovic, N., Isaacs, H. S. & Adzic, R. R. (2016). *ACS Catal.* **6**, 69–76.
Sels, B., De Vos, D., Buntinx, M., Pierard, F., Kirsch-De Mesmaeker, A. & Jacobs, P. (1999). *Nature (London)*, **400**, 855–857.
Song, F. & Hu, X. (2014). *Nat. Commun.* **5**, 1–9.
Tuaev, X., Rudi, S., Petkov, V., Hoell, A. & Strasser, P. (2013). *ACS Nano*, **7**, 5666–5674.
Wang, H., Jang, Y., Huang, B., Sadoway, D. R. & Chiang, Y. (1999). *J. Electrochem. Soc.* **146**, 473–480.
Wilson, B. E., Smyrl, W. H. & Stein, A. (2014). *J. Electrochem. Soc.* **161**, A700–A703.
Winter, M. & Brodd, R. J. (2004). *Chem. Rev.* **104**, 4245–4269.
Woehl, T. J., Jungjohann, K. L., Evans, J. E., Arslan, I., Ristenpart, W. D. & Browning, N. D. (2013). *Ultramicroscopy*, **127**, 53–63.
Wu, J., Shan, S., Petkov, V., Prasai, B., Cronk, H., Joseph, P., Luo, J. & Zhong, C. (2015). *ACS Catal.* **5**, 5317–5327.
Xing, Y. (2004). *J. Phys. Chem. B*, **108**, 19255–19259.
Xue, Y., Liu, J., Chen, H., Wang, R., Li, D., Qu, J. & Dai, L. (2012). *Angew. Chem. Int. Ed.* **51**, 12124–12127.
Young, M. J., Holder, A. M., George, S. M. & Musgrave, C. B. (2015). *Chem. Mater.* **27**, 1172–1180.
Young, M. J., Schnabel, H.-D., Holder, A. M., George, S. M. & Musgrave, C. B. (2016). *Adv. Funct. Mater.* **26**, 7895–7907.
Zhi, M., Xiang, C., Li, J., Li, M. & Wu, N. (2013). *Nanoscale.* **5**, 72–88.
Zhu, G., Prabhudev, S., Yang, J., Gabardo, C. M., Botton, G. A. & Soleymani, L. (2014). *J. Phys. Chem. C*, **118**, 22111–22119.